arXiv:1408.0126v1 [astro-ph.HE] 1 Aug 2014

Jet formation in GRBs: A semi-analytic model of MHD flow in Kerr geometry with realistic plasma injection

Noemie Globus[1] and Amir Levinson[1]

ABSTRACT

We construct a semi-analytic model for MHD flows in Kerr geometry, that incorporates energy loading via neutrino annihilation on magnetic field lines threading the horizon. We compute the double-flow structure for a wide range of energy injection rates, and identify the different operation regimes. At low injection rates the outflow is powered by the spinning black hole via the Blandford-Znajek mechanism, whereas at high injection rates it is driven by the pressure of the plasma deposited on magnetic field lines. In the intermediate regime both processes contribute to the outflow formation. The parameter that quantifies the load is the ratio of the net power injected below the stagnation radius and the maximum power that can be extracted magnetically from the black hole.

1. Introduction

An issue of considerable interest in the theory of gamma-ray bursts (GRBs) is the nature of the gamma-ray emitting jet. The conventional wisdom has been that the jet is produced by a hyper-accreting black hole that results from a neutron star merger in case of short GRBs (Eichler et al. 1989), or the core-collapse of a massive star in case of long GRBs (MacFadyen, Woosley 1999). The black hole is likely to be immersed in a strong magnetic field ($B_H \simeq 10^{15}$G) seeded by the progenitor and advected inwards during the formation of the central engine. Feedback from a rapidly rotating black hole may dominate the torque experienced by the surrounding torus, leading to a state of suspended accretion in long GRBs (van Putten & Ostriker, 2001; van Putten & Levinson 2003), provided that mass loading of magnetic field lines anchored to the disk is, somehow, strongly suppressed (Komissarov & Barkov 2009; Globus & Levinson 2013; hereafter GL13). Rapid heating of the inner regions of the hyper-accretion disk, or the torus in the suspended accretion state if established, leads to prodigious emission of MeV neutrinos (and anti-neutrinos), with luminosities in the range $L_\nu = 10^{51} - 10^{54}$ erg s^{-1}, depending on accretion rate and specific angular momentum a of the black hole (e.g., Popham et al. 1999; Chen & Beloborodov 2007).

In the context of the picture outlined above, two competing jet formation mechanisms have been widely discussed in the literature; magnetic extraction of the spin down power of a Kerr black hole, and outflow formation via neutrino annihilation in the polar region, above the horizon (Paczyński 1990, Levinson & Eichler 1993, Levinson 2006). These two processes are commonly treated under idealized conditions: models of Blandford-Znajek jets usually invoke the force-free limit and ignore loading of magnetic field lines (but c.f., Komissarov & Barkov 2009), whereas models of jets driven by $\nu\bar{\nu}$ annihilation (MacFadyen & Woosley 1999, Fryer & Mészáros 2003) are usually constructed within the pure hydrodynamic limit. In general, however, both processes might be at work, and it is desirable to characterize the interplay between them. The approach undertaken in this paper is to treat $\nu\bar{\nu}$ annihilation in the magnetosphere as external plasma load. It has been shown elsewhere (GL13) that injection of relativistically hot plasma on horizon threading field lines

[1]School of Physics & Astronomy, Tel Aviv University, Tel Aviv 69978, Israel

always leads to the formation of a double-flow structure in the magnetosphere. The plasma inflowing into the black hole carries positive energy that tends to counteract the BZ process. The plasma outflowing to infinity contributes to the total asymptotic power. The question addressed in this paper is how the structure of the MHD flow depends on the details of the plasma injection process.

In a preliminary investigation (GL13), we considered the effect of the load on the activation of the BZ mechanism, assuming that the plasma source is confined to an infinitely thin layer, outside which the MHD flow is ideal and adiabatic. We derived solutions for the inflow section only, and evaluated the critical load above which the BZ process switches off. We then argued that this critical value differentiates magnetically extracted from pressure-driven flows when the injected plasma is relativistically hot. In this paper we extend our analysis to more realistic situations, and obtain solutions of the MHD equations for the entire double-flow structure. We focus on the conditions anticipated in GRBs, and employ a realistic injection profile computed recently by Zalamea & Beloborodov (2011, hereafter ZB11). We identify the different operation regimes, including the intermediate regime where the transition from magnetically extracted to pressure driven flows occurs. We also calculate overloaded solutions for which the BZ process is switch off and compare them with pure hydrodynamic flows derived in a previous study (Levinson & Globus 2013, hereafter LG13).

2. Model

The double-flow structure established in the magnetosphere is illustrated in Figure 1: plasma inflow into the black hole and outflow to infinity are ejected from a stagnation radius, r_{st}, located between the inner and outer light surfaces. The plasma consists of relativistically hot $e^{\pm}$ pairs created via annihilation of MeV neutrinos emitted from the surrounding accretion disk. The exact location of the stagnation surface depends, quite generally, on the energy injection profile, and is treated as an eigenvalue of the MHD equations. The double flow possesses six critical surfaces, corresponding to the characteristic phase speeds of the three MHD waves propagating in the medium: two slow magnetosonic, two Alfvénic and two fast magnetosonic. We consider an infinitely conducting, stationary and axisymmetric flow. In general, the flow is characterized by a stream function $\Psi(r,\theta)$ that defines the geometry of magnetic flux surfaces, and by the following functionals of Ψ: the angular velocity of magnetic field lines $\Omega_F(\Psi)$, the ratio of mass and magnetic fluxes $\eta(\Psi)$, and the energy, angular momentum and entropy per baryon, denoted by $\mathcal{E}(\Psi)$, $\mathcal{L}(\Psi)$ and $s(\Psi)$, respectively. These quantities are given explicitly in Equations (A7)-(A10).

The ideal MHD condition implies that $\Omega_F(\Psi)$ is conserved along magnetic flux tubes, as usual. All other quantities change along streamlines, owing to plasma injection by the external source, according to Equations (A11)-(A14). We assume that in the acceleration zone the plasma is relativistically hot with a negligible baryonic content. We can therefore adopt the equation of state $w = \rho c^2 \bar{h} = 4p$. To simplify the analysis we invoke a split monopole configuration for the magnetic field lines, described by a stream function of the form $\Psi(r,\theta) = \Psi_0(1-\cos\theta)$. The energy, angular momentum and entropy fluxes, Equation (A6), then have only a radial component: $\epsilon^r = \rho\mathcal{E}u^r$, $l^r = \rho\mathcal{L}u^r$, $s^r = \rho s u^r$. Note that $\mathcal{E}$, $\mathcal{L}$ and s diverge in the limit $\rho \to 0$ (baryon-free flow), whereas the corresponding fluxes, ϵ^r, l^r and s^r, remain finite and are well defined also in the baryon-free case. For the relativistic equation of state adopted above the entropy per unit volume is given by $S = \rho s = 4p/kT \propto p^{3/4}$, whereby $s^r \propto u^r p^{3/4}$, hence the pressure p can be used as a free variable instead of S. Since our analysis encompasses the force-free limit, we find it convenient to use ϵ^r, l^r and p as our free variables. With the above simplifications, Equations (A11)-(A13) reduce to:

$$\frac{1}{\sqrt{-g}}\partial_r(\sqrt{-g}\epsilon^r) = -q_t, \tag{1}$$

$$\frac{1}{\sqrt{-g}}\partial_r(\sqrt{-g}l^r) = q_\varphi, \tag{2}$$

$$\frac{3}{4}\partial_r \ln p = -\partial_r \ln(\Sigma u^r) - \frac{u_\alpha q^\alpha}{4pu^r}, \tag{3}$$

here $\sqrt{-g} = \Sigma \sin\theta$, and $\Sigma = r^2 + a^2\cos^2\theta$. This set needs to be augmented by an equation of motion for the velocity u^r. Instead of u^r we use the poloidal velocity $u_p = \sqrt{u^r u_r} = \sqrt{g_{rr}}u^r$. Its rate of change along streamlines is derived in appendix A and can be written in the form,

$$\partial_r \ln u_p = \frac{N_{ad} + N_q}{D}, \tag{4}$$

where N_{ad}, N_q and D are functionals of $\epsilon^r, l^r, p, u_p, \Omega_F$, given explicitly by Equations (A23)-(A25). Equations (1)-(4) form a complete set that governs the structure of the double MHD flow. The solutions for the radial profiles of the free variables ϵ^r, l^r, p, and u_p, depend on the particular choice of the angle θ that characterizes magnetic flux surfaces. The angular velocity $\Omega_F(\theta)$ is given as an input. The energy and angular momentum flow rates per solid angle (along a particular flux surface) are defined, respectively, as:

$$\dot{\mathcal{E}}(r,\theta) \equiv \Sigma\epsilon^r, \quad \dot{\mathcal{L}}(r,\theta) \equiv \Sigma l^r. \tag{5}$$

2.1. Source terms for the process $\nu\bar{\nu} \to e^+e^-$

The energy-momentum deposition rate by the reaction $\nu\bar{\nu} \to e^+e^-$ was computed in a number of works, under different simplifying assumptions (Popham et al. 1999, Chen & Beloborodov 2007, ZB11). In what follows we use the recent analysis by ZB11 which includes general relativistic effects. Following ZB11 we denote by $Q^\alpha_{\nu\bar{\nu}}$ the local energy-momentum deposition rate measured by a zero-angular-momentum observer (ZAMO). In general, those rates are functions of the Boyer-Lindquist coordinates r, θ and φ, as can be seen from Figures 2 and 3 in ZB11. In terms of the metric components defined in appendix A, $g_{\varphi\varphi} = \varpi^2$, $g_{t\varphi} = -\omega g_{\varphi\varphi}$, $g_{tt} = -\alpha^2 + \omega^2 g_{\varphi\varphi}$ and g_{rr}, we have the following relations between the ZAMO rates $Q^\alpha_{\nu\bar{\nu}}$ and the source terms q^α measured by a distant observer: $\alpha q^t = Q^t_{\nu\bar{\nu}}$, $\varpi q^\varphi = Q^\varphi_{\nu\bar{\nu}} + \varpi\omega Q^t_{\nu\bar{\nu}}/\alpha$, $\sqrt{g_{rr}}q^r = Q^r_{\nu\bar{\nu}}$. From that we obtain

$$-q_t = \alpha Q^t_{\nu\bar{\nu}} + \varpi\omega Q^\varphi_{\nu\bar{\nu}}, \tag{6}$$

$$q_\varphi = \varpi Q^\varphi_{\nu\bar{\nu}}, \tag{7}$$

$$u_\alpha q^\alpha = -\alpha u^t Q^t_{\nu\bar{\nu}} + \varpi Q^\varphi_{\nu\bar{\nu}}(u^\varphi - \omega u^t) + u_p Q^r_{\nu\bar{\nu}}. \tag{8}$$

The total power deposited in the magnetosphere can be expressed as,

$$\dot{E}^{tot}_{\nu\bar{\nu}} = \int_{r\geq r_H} \left(\alpha Q^t_{\nu\bar{\nu}} + \varpi\omega Q^\varphi_{\nu\bar{\nu}}\right)\sqrt{-g}drd\theta d\varphi\,. \tag{9}$$

A fit to the numerical results by ZB11 yields: $\dot{E}^{tot}_{\nu\bar{\nu}} \simeq 10^{52}\dot{m}^{9/4}_{acc}\, x^{-4.8}_{mso}$ erg s^{-1} for a black hole mass $M_{BH} = 3M_\odot$, and accretion rates (henceforth measured in units of $M_\odot$ s^{-1}) in the range $0.02 < \dot{m}_{acc} < 1$, where x_{mso} is the radius of the marginally stable orbit in units of $m = GM_{BH}/c^2$.

Unfortunately, ZB11 do not exhibit results for the azimuthal term $Q^\varphi_{\nu\bar{\nu}}$. It is also difficult to fit their result for $Q^r_{\nu\bar{\nu}}$. We shall therefore set $Q^\varphi_{\nu\bar{\nu}} = Q^r_{\nu\bar{\nu}} = 0$. This should not alter much q_t and $u_\alpha q^\alpha$, as the first term on the right hand side of Equations (6) and (8) dominates anyhow. However, for this choice $q_\varphi = 0$,

implying that the angular momentum flow rate, $\dot{\mathcal{L}}(r,\theta) \equiv \Sigma l^r$, is conserved, as readily seen from Equation (2).

For our radial flow model it is sufficient to use the angle-averaged energy deposition rate. We adopt the form

$$Q^t_{\nu\bar{\nu}}(r) = \dot{Q}_0 f(x), \tag{10}$$

where $x = r/m$ is a fiducial radius, and $f(x)$ is normalized such that $f(1) = 1$. From figures 2 and 3 in ZB11 we obtain the approximate profile $f(x) \simeq x^{-b}$, with $b = 4.5$ for a black hole spin parameter $\tilde{a} \equiv a/m = 0.95$, and $b = 3.5$ for $\tilde{a} = 0$. The injected power per solid angle, from the horizon to a given radius x, is then given by

$$\dot{\mathcal{E}}_{\nu\bar{\nu}}(x,\theta) = m^3 \dot{Q}_0 \int_{x_H}^{x} \alpha\Sigma f(x')dx'. \tag{11}$$

The cumulative power distribution in the upper hemisphere ($0 \le \theta \le \pi/2$) is

$$\dot{E}_{\nu\bar{\nu}}(x) = 2\pi \int_0^{\pi/2} \dot{\mathcal{E}}_{\nu\bar{\nu}}(x,\theta)\sin\theta d\theta. \tag{12}$$

It is related to the total power through $\dot{E}^{tot}_{\nu\bar{\nu}} = \dot{E}_{\nu\bar{\nu}}(x=\infty)$. The amount absorbed by the black hole along a particular field line equals the power per solid angle injected in the inflow section (between the horizon and the stagnation radius):

$$\dot{\mathcal{E}}^{in}_{\nu\bar{\nu}}(\theta) = \dot{\mathcal{E}}_{\nu\bar{\nu}}(x_{st},\theta) = m^3\dot{Q}_0 \int_{x_H}^{x_{st}} \alpha\Sigma x^{-b} dx. \tag{13}$$

The rest, $\dot{\mathcal{E}}^{out}_{\nu\bar{\nu}}(\theta) = \dot{\mathcal{E}}^{tot}_{\nu\bar{\nu}}(\theta) - \dot{\mathcal{E}}^{in}_{\nu\bar{\nu}}(\theta)$, where $\dot{\mathcal{E}}^{tot}_{\nu\bar{\nu}}(\theta) \equiv \dot{\mathcal{E}}_{\nu\bar{\nu}}(\infty,\theta)$, emerges at infinity. The total power intercepted by the black hole in one hemisphere is

$$\dot{E}^{in}_{\nu\bar{\nu}} = 2\pi \int_0^{\pi/2} \dot{\mathcal{E}}^{in}_{\nu\bar{\nu}}(\theta)\sin\theta d\theta = \dot{E}_{\nu\bar{\nu}}(x_{st}). \tag{14}$$

A plot of $\dot{E}_{\nu\bar{\nu}}(x)$ (Equation (12)), is exhibited in Figure 2. For our computations we use $b = 4.5$ for a spin parameter $\tilde{a} = 0.95$ (the solid line in Figure 2).

2.2. The load parameter $\kappa(\theta)$

Let us denote by $\dot{\mathcal{E}}_H(\theta) = \dot{\mathcal{E}}(r_H,\theta)$, $\dot{\mathcal{E}}_{st}(\theta) = \dot{\mathcal{E}}(r_{st},\theta)$, and $\dot{\mathcal{E}}_\infty(\theta) = \dot{\mathcal{E}}(\infty,\theta)$ the angular distribution of the power at the horizon, stagnation radius and infinity, respectively, where $\dot{\mathcal{E}}(r,\theta)$ is defined in Equation (5). Integration of Equation (1) yields

$$\dot{\mathcal{E}}_H(\theta) = \dot{\mathcal{E}}_{st}(\theta) - \dot{\mathcal{E}}^{in}_{\nu\bar{\nu}}(\theta), \tag{15}$$

$$\dot{\mathcal{E}}_\infty(\theta) = \dot{\mathcal{E}}_{st}(\theta) + \dot{\mathcal{E}}^{out}_{\nu\bar{\nu}}(\theta), \tag{16}$$

where Equations (6), (10) and (13) have been employed.

Now, the specific energy of the injected plasma is positive, hence $\dot{\mathcal{E}}^{in}_{\nu\bar{\nu}}(\theta) \ge 0$, $\dot{\mathcal{E}}^{out}_{\nu\bar{\nu}}(\theta) \ge 0$, as can be inferred from Equation (11). In the situations envisaged here $\dot{\mathcal{E}}_\infty(\theta) > 0$, but $\dot{\mathcal{E}}_H(\theta)$ can be negative or positive, depending on the load. In the force-free limit $\dot{\mathcal{E}}^{tot}_{\nu\bar{\nu}}(\theta) \to 0$, whereby Equations (15) and (16) yield

$\dot{\mathcal{E}}_\infty(\theta) = \dot{\mathcal{E}}_H(\theta) > 0$. The extracted power per solid angle is given, in this limit, by (Blandford & Znajek, 1977):

$$\dot{\mathcal{E}}_H(\theta) = P_{BZ}(\theta) \equiv \frac{c}{64\pi^3}\alpha_\Omega(1-\alpha_\Omega)\left(\frac{\tilde{a}}{m}\right)^2 \frac{(x_H^2+\tilde{a}^2)\sin^2\theta}{x_H^2(x_H^2+\tilde{a}^2\cos^2\theta)}\Psi_0^2\,, \tag{17}$$

in terms of the black hole spin $\tilde{a}$, magnetic flux Ψ_0, and the dimensionless parameter $\alpha_\Omega = \Omega_F/\omega_H$. In general $\dot{\mathcal{E}}_H(\theta) < P_{BZ}(\theta)$, as readily seen from Equation (15).

Henceforth, we shall quantify the load on a specific streamline θ by the parameter

$$\kappa(\theta) \equiv \frac{\dot{\mathcal{E}}^{in}_{\nu\bar{\nu}}(\theta)}{P_{BZ}(\theta)}. \tag{18}$$

At $\kappa(\theta) << 1$ the flow along the streamline θ is nearly force-free. At $\kappa(\theta) >> 1$ the flow is nearly hydrodynamic, whereby $\dot{\mathcal{E}}_{st}(\theta) \simeq 0$ and $\dot{\mathcal{E}}_H(\theta) \simeq -\dot{\mathcal{E}}^{in}_{\nu\bar{\nu}}(\theta) < 0$, namely the energy injected below the stagnation radius on the flux surface θ is completely absorbed by the black hole. As shown below, the transition between the two regimes occurs, in general, at $\kappa(\theta) \simeq 1$.

3. Integration method

In general, the double flow must pass smoothly through 6 critical surfaces. Solutions that satisfy this requirement can be obtained, in principle, only if the trans-field equation is solved simultaneously with Equations (A11)-(A13), as the exact location of the critical surfaces is contingent upon the actual shape of the magnetic surfaces. Such an analysis is beyond the scope of this paper. Fixing the geometry of magnetic field lines renders the system of MHD equations, Eqs. (1)-(4), over constrained. The reason is that there are 4 regularity conditions (the regularity conditions at the inner and outer Alfvén surfaces are automatically satisfied), but only 3 adjustable parameters; the location of the stagnation point, r_{st}, at which $u_p = 0$, and the values of ϵ^r and p at r_{st}, henceforth denoted by ϵ^r_{st}, and p_{st}, respectively. The value of the angular momentum flux at r_{st} is related to ϵ^r_{st} through the Bernoulli condition, Equation (A31): $l^r_{st} = \Omega_F^{-1}\epsilon^r_{st}$. Since we are interested in determining the energy flux on the horizon, we seek solutions that are regular on all 3 inner surfaces, and on the outer slow magnetosonic surface, but not necessarily on the outer fast magnetosonic surface. In practice we find that any solution that crosses the outer slow magnetosonic surface, is also regular on the outer Alfvén surface.

Our strategy is to start with some initial guess for the three adjustable parameters, r_{st}, ϵ^r_{st}, and p_{st}, whereupon Equations (1)-(4) are integrated numerically from r_{st} inwards to the horizon, and outwards to the outer Alfvén surface, along a given field line θ. The integration is repeated many times, where in each run the values r_{st}, ϵ^r_{st}, p_{st} are readjusted until a solution that crosses the desired critical points smoothly is obtained. In all the examples presented below we neglected the change in linear and angular momentum owing to plasma injection, that is, we set $Q^\varphi_{\nu\bar{\nu}} = Q^r_{\nu\bar{\nu}} = 0$ in Equations (6)-(9). Equation (2) then readily yields $\dot{\mathcal{L}} = \Sigma l^r = \text{const}$. The black hole spin $\tilde{a}$, angular velocity of the streamlines Ω_F, and load parameter κ are given as input parameters. In practice, however, κ cannot be determined a priori, since r_{st} is unknown. We therefore use instead of κ the dimensionless parameter $\tilde{p}_B \equiv \Psi_0^2 c/(32\pi^3\dot{Q}_0 m^5)$ as an indicator for the load. Once a solution is obtained and r_{st} is determined, κ is computed by employing Equations (13), (17) and (18).

4. Results

The family of solutions can be divided into two classes that are distinguished by the sign of the energy flux on the horizon, ϵ^r_H. This devision is dictated by the load parameter $\kappa(\theta)$, as discussed further below (Figure 4). We find that in case of underloaded solutions, defined as those for which $\kappa(\theta) << 1$, the specific energy is negative in the entire region encompassed by the plasma inflow (below the stagnation radius), including the horizon, whereby $\epsilon^r_H > 0$. In case of overloaded solutions ($\kappa(\theta) >> 1$) we find $\epsilon^r_H < 0$. Interestingly, the energy flux of overloaded solutions changes sign at some radius below the stagnation point, implying that there is still a region where the specific energy of the plasma inflow is negative. Typical examples are shown in Figure 3, where the velocity profiles (left panel) and the corresponding energy fluxes (right panel) of underloaded ($\kappa = 10^{-5}$) and overloaded ($\kappa = 20$) equatorial flows are exhibited, for a black hole spin parameter $\tilde{a} = 0.95$, and an energy deposition profile $f(x) = x^{-4.5}$. In the right panel we also exhibit solutions with $\kappa = 0.4$, 1, 6, and $\kappa = \infty$ (a purely hydrodynamic flow), that are not shown in the left panel for clarity. As seen, the energy flux of the underloaded solutions is positive everywhere, whereas that of overloaded solutions changes sign below the stagnation radius. The location r_0 at which $\dot{\mathcal{E}}(r_0, \theta) = 0$ approaches r_{st} as $\kappa(\theta) \to \infty$. We think that this peculiar behavior stems from the fact that in the regime $\Omega_F < \omega_H$ the Poynting flux measured by a distant observer is always driven by the black hole (i.e., by frame dragging). To elucidate this point we employ Equation (A16) to obtain the Poynting flux on the horizon:

$$\left(\frac{F^{r\theta}F_{\theta t}}{4\pi}\right)_H = -\frac{\varpi_H^2\Omega_F(\omega_H - \Omega_F)}{M_H^2 + \varpi_H^2(\omega_H - \Omega_F)^2}(\epsilon^r_H - \omega_H l^r_H). \tag{19}$$

Now, $\epsilon^r_H - \omega_H l^r_H = \rho_H u^r_H(\mathcal{E}_H - \omega_H \mathcal{L}_H)$ is always negative, since the ZAMO energy is always positive, viz., $\mathcal{E}^{ZAMO} = \mathcal{E} - \omega\mathcal{L} > 0$, and $u^r_H < 0$. Thus, for any value of the load parameter, the electromagnetic flux on the horizon is positive if $\omega_H > \Omega_F$. Note also that in the force-free limit $M_H^2 \to 0$, and (19) reduces to the familiar result, $\epsilon^r_H = (F^{r\theta}F_{\theta t})_H/4\pi$, whereas in the pure hydrodynamic case $M_H^2 \to \infty$ and the Poynting flux vanishes, as expected. Figure 4 shows the electric current, $I = \alpha\varpi B_\varphi$, for two overloaded solutions, and it is seen that it never changes sign. We find that this is true in general in the regime $0 < \Omega_F < \omega_H$, implying that for any value of κ there is a continuous flow of Poynting energy from the horizon outwards, against the inflow of injected plasma. In particular, at the stagnation radius $B_\varphi(r_{st}) < 0$, and from Equation (A7) we obtain [1]

$$\epsilon^r_{st} = -\left(\frac{\varpi\Omega_F B_\varphi B_r}{4\pi\sqrt{g_{rr}}}\right)_{st} = \left(\frac{F^{r\theta}F_{\theta t}}{4\pi}\right)_{st} > 0. \tag{20}$$

Since for overloaded solutions $\epsilon^r_H < 0$, it is evident that the energy flux must vanish at some radius $r < r_{st}$, as seen in the right panel of Figure 3. Our interpretation is that the outward flow of electromagnetic energy driven by the black hole is counteracted by an inward flow of kinetic energy injected on magnetic flux tubes. When the latter exceeds the former the net energy flux becomes negative. For $\kappa(\theta) << 1$ this never happens, implying energy extraction from the black hole. For $\kappa(\theta) >> 1$ this happens close to the stagnation radius, and since $\epsilon^r_H < 0$ we infer that the black hole is being fed by the energy of the overloaded inflow (i.e., the energy injected below the stagnation radius).

Figure 5 displays the dependence of the outflow power on the load in the regime where rotational energy extraction is switched on, viz., $\epsilon^r_H > 0$. For reference, powers are normalized to the equatorial BZ power,

[1] This point was not properly understood in GL13. The claim made there, that for overloaded solutions B_φ must vanish at r_{st} is incorrect. However, the conclusion regarding the activation of the BZ process remains valid, as confirmed in the present analysis.

$P_{BZ}(\pi/2)$. The horizontal axis gives values of the parameter $\dot{\mathcal{E}}^{in}_{\nu\bar{\nu}}(\theta)/P_{BZ}(\pi/2)$, which for the equatorial flow ($\theta = \pi/2$) is just the load parameter $\kappa(\theta)$ defined in Equation (18). For other streamlines, the load parameter is obtained by multiplying values on the horizontal axis by the factor $P_{BZ}(\pi/2)/P_{BZ}(\theta)$. The dashed lines delineate the normalized power extracted from the black hole, $\dot{\mathcal{E}}_H(\theta)/P_{BZ}(\pi/2)$, and the solid lines the asymptotic power at infinity, $\dot{\mathcal{E}}_\infty(\theta)/P_{BZ}(\pi/2)$. These lines are essentially the locus of solutions obtained from the numerical integration of Equations (1)-(4). Specific cases are indicated by the symbols; the circles correspond to solutions for which $\Omega_F = \omega_H/2$ and the triangles to solutions for which $\Omega_F = \omega_H/4$. As seen, the effect of the load is highly insensitive to the value of Ω_F, even though the structure of the flow does depend on this parameter (see Figure 6 below). This analysis confirms that the transition from underloaded to overloaded flows occurs at $\kappa(\theta) \simeq 1$. We also computed solutions for different black hole spins, and found the same behavior (see, for example, Figure 4 in GL13). One caveat is the possibility of a nonlinear feedback of the load on the magnetic flux in the vicinity of the horizon. Such a feedback may, in principle, change somewhat the activation condition, but not in a drastic way. It may be possible to test it using numerical simulations.

As explained above, in our model the angular velocity Ω_F is given as an input. In reality it is determined by global conditions. For nearly force-free flows numerical simulations indicate that $\Omega_F \simeq \omega_H/2$. We therefore used this value for the underloaded solutions. However, when the inertia of the injected plasma becomes important, it is likely to affect Ω_F. To study how the properties of the flow depend on this parameter, we sought solutions with different values of $\Omega_F(\theta)$, but the same value of $\kappa(\theta)$. An example is presented in Figure 6, and it is seen that while the velocity profile depends on Ω_F, the power profile is insensitive to the choice of this parameter. In particular, it does not affect at all the activation condition. We find this trend is quite general, and therefore conclude that the result exhibited in Figure 5 is robust.

5. Conclusion

We constructed a semi-analytic model for the double-transonic flow established in the magnetosphere of a Kerr black hole under conditions anticipated in GRBs, incorporating plasma deposition on magnetic field lines via annihilation of MeV neutrinos emitted by the surrounding hyper-accretion flow. We examined the effect of energy loading on the properties of the flow, and identified the different operation regimes. We find that magnetic extraction of the black hole spin energy ensues, as long as the power deposited below the stagnation radius separating the inflow and outflow sections is smaller than the force-free BZ power. The transition from underloaded flows that are powered by the black hole spin energy, to overloaded flows that are powered by the neutrino source is continuous, as seen in Figure 5.

To relate the load parameter derived in Equation (18) to the accretion rate $\dot{m}_{acc}$ (henceforth measured in units of $M_\odot$ s^{-1}), we employ the scaling relation derived in ZB11. As mentioned above, their analysis, that exploit an advanced disk model, yields a total energy deposition rate of

$$\dot{E}^{tot}_{\nu\bar{\nu}} \simeq 10^{52}\,(M_{BH}/3M_\odot)^{-3/2}\,\dot{m}^{9/4}_{acc}\,x^{-4.8}_{mso} \quad \text{erg s}^{-1}, \tag{21}$$

for accretion rates in the range $0.02 < \dot{m}_{acc} < 1$, where x_{mso} is the radius of the marginally stable orbit in units of m. Combining the latter result with the activation condition derived from Figure 5, and using the angle averaged energy deposition rate, yields a rough estimate for the accretion rate at which a transition from underloaded to overloaded solutions occurs:

$$\dot{m}_c \simeq 1\left(\frac{M_{BH}}{3M_\odot}\right)^{-2/9}\left(\frac{\Psi_0}{10^{28}\,\text{G cm}^2}\right)^{8/9} f(\tilde{a}). \tag{22}$$

Here Ψ_0 is the magnetic flux accumulated in the vicinity of the horizon, and the function $f(\tilde{a})$ is displayed in Figure 7. According to this relation, when $\dot{m}_{acc} < \dot{m}_c$ the outflow is powered by the BZ process, whereas for $\dot{m}_{acc} > \dot{m}_c$ it is driven by the neutrino source. In reality, the magnetic flux Ψ_0 should also depend on the accretion rate, however, the sensitivity of this relation to the assumptions underlying the specific disk model adopted for its calculation renders it highly uncertain. Furtheremore, the presence of sufficiently strong magnetic field in the inner disk regions may affect the neutrino luminosity. For illustration, we use the disk model of Chen & Beloborodov (2007) to estimate the magnetic flux. Unfortunately, it is difficult to derive scaling relations from the results presented in this paper, but from Figures 1 and 2 there we obtained $\Psi_0 \sim 2 \times 10^{28}\sqrt{\xi_B}$ G cm^2 for a black hole mass $M_{BH} = 3M_\odot$, angular momentum $\tilde{a} = 0.95$, viscosity parameter $\alpha_{vis} = 0.1$, and accretion rate $\dot{m}_{acc} = 0.2$, assuming that the magnetic pressure in the inner regions of the disk is a fraction ξ_B of the total pressure. For this choice we infer that with ξ_B on the order of a few percents, as naively expected, the transition from underloaded to overloaded flows may occur at accretion rates $\dot{m}_{acc} > 0.1$ or so. We emphasize that this estimate is highly uncertain.

The above results may also have some implications for the jet structure. To be concrete, the dependence of the activation condition on the inclination angle θ of magnetic surfaces (see Figure 5), and the approximate uniformity of the angular distribution of the energy deposition rate indicated in Figures 2 and 3 of ZB11, suggest that for accretion rates $\dot{m}_{acc} \lesssim \dot{m}_c$, and unless the magnetic flux near horizon is extremely high, the outflow produced in the polar region may consist of an inner core inside which the power is dominated by the thermal energy of the hot plasma, and outside which it is dominated by the Poynting flux driven by frame dragging.

This research was supported by a grant from the Israel Science Foundation no. 1277/13

A. Derivation of the flow equations

The stress-energy tensor of a magnetized fluid takes the form,

$$T^{\alpha\beta} = \bar{h}\rho c^2 u^\alpha u^\beta + p g^{\alpha\beta} + \frac{1}{4\pi}\left(F^{\alpha\gamma}F^\beta_\gamma - \frac{1}{4}g^{\alpha\beta}F^2\right), \tag{A1}$$

here u^α is the four-velocity measured in units of c, $\bar{h} = (\rho c^2 + e_{int} + p)/\rho c^2$ the dimensionless specific enthalpy, ρ the baryonic rest-mass density, p the pressure, and $g_{\mu\nu}$ the coefficients of the metric tensor of the Kerr spacetime. In the following we use geometrical units ($c = G = 1$), unless otherwise stated, and express the Kerr metric in the regular Boyer-Lindquist coordinates, $ds^2 \equiv g_{\mu\nu}dx^\mu dx^\nu$ with the non-zero metric coefficients given by: $g_{rr} = \Sigma/\Delta$, $g_{\theta\theta} = \Sigma$, $g_{\varphi\varphi} \equiv \varpi^2 = A\sin^2\theta/\Sigma$, $g_{tt} = -\alpha^2 + \omega^2 g_{\phi\phi}$, $g_{t\phi} = -\omega g_{\phi\phi}$, in terms of $\Delta = r^2 + a^2 - 2mr$, $\Sigma = r^2 + a^2\cos^2\theta$, $A = (r^2+a^2)^2 - a^2\Delta\sin^2\theta$, $\alpha = \sqrt{\Sigma\Delta/A}$, and $\omega = 2mra/A$. The parameters m and a are the mass and specific angular momentum per unit mass of the hole, α is the time lapse and ω the frame dragging potential between a zero-angular-momentum observer (ZAMO) and an observer at infinity. The angular velocity of the black hole is defined as the value of ω on the horizon, viz., $\omega_H \equiv \omega(r = r_H) = a/(2mr_H)$, here $r_H = m + \sqrt{m^2 - a^2}$ is the radius of the horizon, obtained from the condition $\Delta_H = 0$.

The dynamics of the flow is governed by the energy-momentum equations:

$$\frac{1}{\sqrt{-g}}(\sqrt{-g}T^{\alpha\beta})_{,\alpha} + \Gamma^\beta_{\mu\nu}T^{\mu\nu} = q^\beta, \tag{A2}$$

mass conservation:

$$\frac{1}{\sqrt{-g}}\partial_\alpha(\sqrt{-g}\rho u^\alpha) = q_n, \tag{A3}$$

and Maxwell's equations:

$$F^{\beta\alpha}_{;\alpha} = \frac{1}{\sqrt{-g}}(\sqrt{-g}F^{\beta\alpha})_{,\alpha} = 4\pi j^\beta, \tag{A4}$$

$$F_{\alpha\beta,\gamma} + F_{\beta\gamma,\alpha} + F_{\gamma\alpha,\beta} = 0, \tag{A5}$$

subject to the ideal MHD condition $F^{\mu\nu}u_\nu = 0$. Here, q^β denotes the source terms associated with energy-momentum transfer by an external agent, q_n is a particle source, and $\Gamma^\beta_{\mu\nu}$ denotes the affine connection.

The energy, angular momentum and entropy fluxes, can be expressed explicitly as

$$\epsilon^a \equiv -T^a_t = \rho u^a \mathcal{E}, \quad l^a \equiv T^a_\varphi = \rho u^a \mathcal{L}, \quad s^a = (\rho/m_N)u^a s, \tag{A6}$$

in terms of the energy per baryon,

$$\mathcal{E} = -\bar{h}u_t - \frac{\alpha\varpi\Omega_F}{4\pi\eta}B_\varphi, \tag{A7}$$

angular momentum per baryon,

$$\mathcal{L} = \bar{h}u_\varphi - \frac{\alpha\varpi B_\varphi}{4\pi\eta}, \tag{A8}$$

and the entropy per baryon s, where

$$\Omega_F = v^\varphi - \frac{v_p B_\varphi}{\varpi B_p} \tag{A9}$$

is the angular velocity of magnetic field lines,

$$\eta = \frac{\rho u_p}{B_p} \tag{A10}$$

is the ratio of mass and magnetic fluxes, and the index a runs over r and θ. In the above equations $u_p = \pm(u_r u^r + u_\theta u^\theta)^{1/2}$ is the poloidal velocity, where the plus sign applies to outflow lines and the minus sign to inflow lines, $v_p = u_p/\gamma$, with $\gamma = u^t\alpha$ being the Lorentz factor measured by a ZAMO, $v^\varphi = u^\varphi/u^t$, $B_p = (B_r^2 + B_\theta^2)^{1/2}/\alpha$ is the redshifted poloidal magnetic field, and $B_r = F_{\theta\varphi}/\sqrt{A}\sin\theta$, $B_\theta = \sqrt{\Delta}F_{\varphi r}/\sqrt{A}\sin\theta$ and $B_\varphi = \sqrt{\Delta}F_{r\theta}/\Sigma$ the magnetic field components measured by a ZAMO (see van Putten and Levinson 2012 for details). Note that with our sign convention the value of η is defined to be positive on outflow lines and negative on inflow lines.

For a stationary and axisymmetric ideal MHD flow, Equations (A2)-(A5) can be reduced to (GL13)

$$\frac{1}{\sqrt{-g}}\partial_a(\sqrt{-g}\epsilon^a) = -q_t, \tag{A11}$$

$$\frac{1}{\sqrt{-g}}\partial_a(\sqrt{-g}l^a) = q_\varphi, \tag{A12}$$

$$\frac{kT}{\sqrt{-g}}\partial_a(\sqrt{-g}s^a) = -u_a q^\alpha, \tag{A13}$$

$$u^a\partial_a\eta = \frac{u_p q_n}{B_p}, \tag{A14}$$

$$u^a\partial_a\Omega(\Psi) = 0. \tag{A15}$$

It can be readily seen that for $q_n = q^\mu = 0$, the quantities $\Omega(\Psi)$, $\mathcal{E}(\Psi)$, $\mathcal{L}(\Psi)$, $\eta(\Psi)$ and $s(\Psi)$ are conserved on magnetic flux surfaces $\Psi(r,\theta)$ =const, as is well known (e.g., Camenzind 1986).

From (A7)-(A10) we obtain the expressions:

$$B_\varphi = -\frac{4\pi\eta\mathcal{E}}{\alpha\varpi}\,\frac{\alpha^2\tilde{L} - \varpi^2(\Omega_F-\omega)(1-\tilde{L}\omega)}{k_0 - M^2} \tag{A16}$$

$$u^t = \frac{\mathcal{E}}{\bar{h}}\,\frac{\alpha^2(1-\Omega_F\tilde{L}) - M^2(1-\omega\tilde{L})}{\alpha^2\,(k_0-M^2)}, \tag{A17}$$

$$u^\varphi = \frac{\mathcal{E}}{\bar{h}}\frac{\alpha^2\Omega_F(1-\Omega_F\tilde{L}) - M^2\omega(1-\omega\tilde{L}) - M^2\tilde{L}\alpha^2\varpi^{-2}}{\alpha^2\,(k_0-M^2)}\,, \tag{A18}$$

here $\tilde{L} = \mathcal{L}/\mathcal{E}$, M as the poloidal Alfvénic Mach number, defined through $M^2 \equiv 4\pi\bar{h}\eta^2c^2/\rho = u_p^2/u_A^2$, and $u_A^2 = B_p^2/(4\pi\bar{h}\rho c^2)$. Combining the latter relations with the normalization condition $u^\alpha u_\alpha = -1$ yields the Bernoulli equation (Camenzind, 1986; Takahashi et al. 1990):

$$u_p^2 + 1 = \left(\frac{\mathcal{E}}{\bar{h}}\right)^2 \frac{k_0k_2 - 2k_2M^2 - k_4M^4}{(k_0-M^2)^2}\,, \tag{A19}$$

where

$$k_0 = \alpha^2 - \varpi^2\left(\Omega_F-\omega\right)^2, \tag{A20}$$

$$k_2 = (1-\tilde{L}\Omega)^2, \tag{A21}$$

$$k_4 = \frac{\tilde{L}^2}{\varpi^2} - \frac{(1-\tilde{L}\omega)^2}{\alpha^2}\,. \tag{A22}$$

In terms of the free variables, ϵ^r, l^r, p, used in our integration we have: $\eta\mathcal{E} = \sqrt{\Sigma}\epsilon^r/(\sqrt{\Delta}B_p)$, and $\mathcal{E}/\bar{h} = \epsilon^r/(4pu^r)$, $\tilde{L} = l^r/\epsilon^r$.

The equation of motion (4) is obtained upon differentiating Equation (A19) along a given streamline, using Equations (A11)-(A13) with the source terms $q_t = -\alpha\dot{Q}_0 f(x)$, $q_\phi = 0$ and $u_\alpha q^\alpha = u^t q_t$, which are derived in section 2.1, and noting that in the split monopole geometry, the redshifted poloidal field reduces to $B_p = \Psi_0/(2\pi\sqrt{\Sigma\Delta})$, the poloidal velocity is $u_p = \sqrt{\Sigma/\Delta}u^r$, and the convective derivative reduces to $u^\alpha\partial_\alpha = u^r\partial_r = \sqrt{\Delta/\Sigma}u_p\partial_r$. This yields the following expressions for the functionals D, N_{ad} and N_q in Equation (4):

$$D = \left(k_0-M^2\right)^2\left[\left(u_p^2-c_s^2\right)\left(k_0-M^2\right) + \left(\frac{\mathcal{E}}{\bar{h}}\right)^2 M^4\frac{(k_0k_4+k_2)}{\left(k_0-M^2\right)^2}\right], \tag{A23}$$

$$N_{ad} = \left[-\left(1+u_p^2\right)\left(k_0-M^2\right)^3c_s^2 + \left(\frac{\mathcal{E}}{\bar{h}}\right)^2 M^4\left(k_0k_4+k_2\right)\right]\partial_x\ln B_p \tag{A24}$$

$$-\frac{3}{16}\left(\frac{\mathcal{E}}{\bar{h}}\right)^2\left[M^4\left(k_0-M^2\right)\partial_x k_{ad} + \left(k_0k_2 - 3k_2M^2 - 2k_4M^4\right)\partial_x k_0\right],$$

$$N_q = -\frac{3\,q_t}{2\,\epsilon^r}\left(\frac{\mathcal{E}}{\bar{h}}\right)^2\left(k_0-M^2\right)\left[\left(k_0-2M^2\right)\left(1-\Omega_F\tilde{L}\right) + \frac{M^4}{\alpha^2}(1-\omega\tilde{L})\right]$$

$$-\frac{2\,q_t}{\epsilon^r}\left(\frac{\mathcal{E}}{\bar{h}}\right)^4\left[-k_4M^6 - k_2\left(k_0^2 - 3k_0M^2 + 3M^4\right)\right]\frac{\alpha^2(1-\Omega_F\tilde{L}) - M^2(1-\omega\tilde{L})}{\alpha^2\,(k_0-M^2)}, \tag{A25}$$

where the derivatives are defined by

$$\partial_x k_0 = \partial_x(\alpha^2) - (\Omega_F - \omega)^2\,\partial_x(\varpi^2) + 2\varpi^2\,(\Omega_F - \omega)\,\partial_x\omega, \tag{A26}$$

$$\partial_x k_{ad} = \frac{2}{\alpha^2}(1-\tilde{L}\omega)^2\partial_x \ln\alpha + \frac{2\tilde{L}\omega}{\alpha^2}(1-\tilde{L}\omega)\partial_x \ln\omega - \frac{2\tilde{L}^2}{\varpi^2}\partial_x \ln\varpi\,. \tag{A27}$$

A.1. The stagnation point

At the stagnation point $x = x_{st}$, where $u_p = 0$, Equations (1)-(4) with $q_\varphi = 0$ yield:

$$\partial_x u_{p_{|_{x=x_{st}}}} = -\frac{(\Sigma q_t)_{st}}{4p_{st}\alpha_{st}(k_{0st}\,A_{st})^{1/2}}, \tag{A28}$$

$$\partial_x(\Sigma\epsilon^r)_{|_{x=x_{st}}} = -(\Sigma q_t)_{st}\,, \tag{A29}$$

$$\frac{3}{4}\partial_x \ln(p)_{|_{x=x_{st}}} = -\frac{x_{st}-1}{\Delta_{st}} - \frac{x_{st}}{\Sigma_{st}} - \frac{\Sigma_{st}^2 f(x_{st})\epsilon^r_{st}(1-\omega_{st}/\Omega_F)}{8p_{st}\alpha_{st}k_{0st}\tilde{p}_B}, \tag{A30}$$

where $-(\Sigma q_t)_{st} = \alpha_{st}\Sigma_{st}\dot{Q}_0 f(x_{st})$, and the parameter $\tilde{p}_B \equiv \Psi_0^2 c/(32\pi^3\dot{Q}_0 m^5)$ is an indicator for the load.

The Bernoulli condition can be rewritten

$$(1-\tilde{L}_{st}\Omega_F)\frac{\epsilon^r_{st}}{(4pu^r)_{st}} = \sqrt{k_{0st}}\,, \tag{A31}$$

implying $\tilde{L}_{st}\Omega_F = 1$, since as we have shown, there is always extraction of angular momentum from the black hole so that $\epsilon^r_{st} > 0$.

A.2. The Alfvén surfaces

The location of the Alfvén surfaces is defined by the roots of the denominator in Equations (A16)-(A18), $M_A^2 = k_{0A} = \alpha_A^2 - \varpi_A^2(\Omega_F - \omega_A)^2$, here the subscript A denotes values on this surface. The latter equation has two roots, corresponding to the inner and outer Alfvén surfaces. The requirement that B_φ, u^t and u^φ in Equations (A16)-(A18) are continuous there imposes a condition on the ratio of the ZAMO energy, $\mathcal{E}^{ZAMO} = \mathcal{E} - \omega\mathcal{L}$, and the energy $\mathcal{E}$ of an observer at infinity:

$$\left(\frac{\mathcal{E}}{\mathcal{E}^{ZAMO}}\right)_A = 1 - \alpha_A^{-2}\varpi_A^2\omega_A(\omega_A - \Omega_F). \tag{A32}$$

In the regime where the BZ process is activated, $\epsilon^r_H = \rho u^r\mathcal{E} > 0$, and we must have $\mathcal{E} < 0$ anywhere below the stagnation radius where $u^r < 0$, and in particular at the inner Alfvén point (IA). Since the ZAMO energy is always positive, the latter condition, combined with Equation (A32), readily implies $\omega_{IA} > \Omega_F$, and defines the range of Alfvén radii that are permitted for energy extraction:

$$\frac{\alpha_{IA}}{\sqrt{\omega_{IA}(\omega_{IA}-\Omega_F)}} < \varpi_{IA}. \tag{A33}$$

The shaded area in Figure 8 marks this range for solutions with $\Omega_F = \omega_H/2$. In the outflow section all energies are positive, yielding $\omega_{OA} < \Omega_F$, and

$$\frac{\alpha_{OA}}{\sqrt{\omega_{OA}(\omega_{OA}-\Omega_F)}} > \varpi_{OA}, \tag{A34}$$

at the outer Alfvén point (OA).

B. Pure hydrodynamic flows

The equations governing a purely hydrodynamic flow can be obtained formally from the MHD equations derived above upon taking the limit $M^2 \to \infty$:

$$(u_p^2 - c_s^2)\partial_x \ln u_p = N_{ad} + N_q, \tag{B1}$$

$$N_{ad} = (1+u_p^2)c_s^2\left(\frac{x}{\Sigma}+\frac{x-1}{\Delta}\right) - \left(\frac{\mathcal{E}}{\bar{h}}\right)^2 \frac{3\partial_x k_{ad}}{4}, \tag{B2}$$

$$N_q = -\frac{3\,q_t}{2\alpha^2\epsilon^r}(1-\tilde{L}\omega)\left(\frac{\mathcal{E}}{\bar{h}}\right)^2\left[1+\left(\frac{\mathcal{E}}{\bar{h}}\right)^2\frac{4\,k_4}{3}\right]. \tag{B3}$$

$$\frac{3}{4}\partial_x \ln\tilde{p} = -\partial_x \ln u_p - \frac{x}{\Sigma} - \frac{x-1}{\Delta} - \frac{q_t(1-\tilde{L}\omega)}{\alpha^2\epsilon^r}\left(\frac{\mathcal{E}}{\bar{h}}\right)^2, \tag{B4}$$

$$\partial_x(\Sigma\epsilon^r) = -\Sigma q_t\,, \tag{B5}$$

where now $\tilde{L}$ is a free parameter that describes the family of solutions, $\tilde{p} = p/\dot{Q}_0 t_d$ is the normalized pressure, with $t_d = GM_{BH}/c^3$. The Bernoulli condition (A31) implies, in this limit, $\epsilon^r_{st} = 0$, as expected in the absence of magnetic fields. It can be readily shown that when $M^2 \to \infty$ the slow-magnetosonic and Alfven speeds approach zero, whereas the fast-magnetosonic speed approaches the sound speed, $c_s = 1/\sqrt{2}$. Consequently, the above system of equations has critical points at $u_p = \pm c_s$, as can be directly verified.

The regularity conditions at the sonic points, obtained from Equations (B2) and (B3), read:

$$2\left(\frac{x_{c1}}{\Sigma_{c1}}+\frac{x_{c1}-1}{\Delta_{c1}}\right) + 3\frac{(\partial_x k_{ad})_{c1}}{k_{4,c1}} = -\sqrt{\frac{3}{-k_{4,c1}}}\frac{\sqrt{\Sigma_{c1}}f(x_{c1})(1-\tilde{L}_{c1}\omega_{c1})}{\tilde{p}_{c1}\sqrt{\Delta_{c1}}\alpha_{c1}}, \tag{B6}$$

$$2\left(\frac{x_{c2}}{\Sigma_{c2}}+\frac{x_{c2}-1}{\Delta_{c2}}\right) + 3\frac{(\partial_x k_{ad})_{c2}}{k_{4,c2}} = +\sqrt{\frac{3}{-k_{4,c2}}}\frac{\sqrt{\Sigma_{c2}}f(x_{c2})(1-\tilde{L}_{c2}\omega_{c2})}{\tilde{p}_{c2}\sqrt{\Delta_{c2}}\alpha_{c2}}, \tag{B7}$$

denoting the sonic point of the inflow (outflow) by $x_{c1}(x_{c2})$, and noting that $u_p = -1/\sqrt{2}$ at x_{c1}, and $u_p = 1/\sqrt{2}$ at x_{c2}. As seen, the existence of two sonic points, that is, $x_{c1} \neq x_{c2}$, is a consequence of energy injection. When $f(x) = 0$ the solutions of (B6) and (B7) merge, and the system has only one critical point, for either an inflow or an outflow, depending on the boundary conditions.

At the stagnation point, $x = x_{st}$, the above equations yield

$$\partial_x u_{p|_{x=x_{st}}} = \frac{f(x_{st})\sqrt{\Sigma_{st}}(1-\tilde{L}_{st}\omega_{st})}{4\tilde{p}_{st}\sqrt{\Delta_{st}}\alpha_{st}\sqrt{-k_{4,st}}}, \tag{B8}$$

$$\partial_x(\Sigma\epsilon^r)_{|_{x=x_{st}}} = -(\Sigma q_t)_{st}\,, \tag{B9}$$

$$\partial_x \ln(\tilde{p})_{|_{x=x_{st}}} = \frac{2}{k_{4,st}}(\partial_x k_{ad})_{st}, \tag{B10}$$

where $\tilde{p}_{st} = \tilde{p}(x_{st})$ is the normalized stagnation pressure. Thus, for a given choice of $f(x)$ the solution is fully determined once x_{st} and $\tilde{p}_{st}$ are known, since $\epsilon^r_{st} = 0$.

REFERENCES

Blandford, R. D. & Znajek, R. L. 1977, MNRAS, 179, 433

Camenzind, M. 1986, ApJ, 162, 32

Chen, W-X. & Beloborodov, A. 2007, ApJ, 657, 383

Eichler, D., Livio, M., Piran, T. & Schramm, D. N. 1989, Nature, 340, 126

Fryer, C. L., & Mészáros, P. 2003, ApJ, 588, L25

Globus, N. & Levinson, A 2013, Phys. Rev. D, 88, 4046

Komissarov, S. & Barkov, M. 2009, MNRAS, 397, 1153

Levinson, A. 2006, ApJ, 648, 510

Levinson, A. & Eichler, D. 1993, ApJ, 418, 386

Levinson, A & Globus, N. 2013, ApJ, 770, 159

MacFadyen, A. I. & Woosley, S. E. 1999, ApJ, 524, 262

Paczyński, B. 1990, ApJ, 363, 218

Popham, R., Woosley, S. E., & Fryer, C. 1999, ApJ, 518, 356

Takahashi, M., Nitta, S., Tatematsu, Y. & Tomimatsu, A. 1990, ApJ, 363, 206

Thorne, K. S., MacDonald, D. A. & Price, R. H. 1986, Black Holes: The Membrane Paradigm (Yale University Press)

van Putten, M. H. P. M. & Levinson, A. 2003, ApJ, 584, 937

van Putten, M. H. P. M. & Levinson, A. 2012, Relativistic Astrophysics of the Transient Universe (Cambridge University Press)

van Putten, M. H. P. M. & Ostriker, E. C. 2001, ApJ, 552, 31

Zalamea, I. & Beloborodov, A. 2011, MNRAS, 410, 2302

This preprint was prepared with the AAS LaTeX macros v5.2.

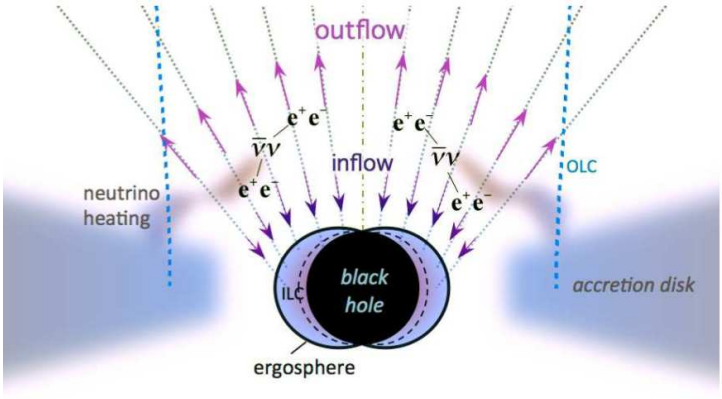

Fig. 1.— Illustration of the double-transonic flow model.

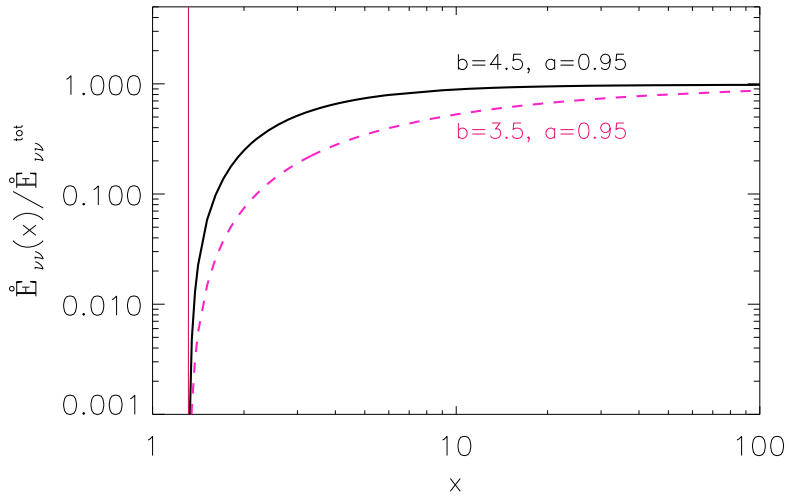

Fig. 2.— Net power deposited on magnetic field lines via neutrino annihilation as a function of radius x (Equation (12)), for two different injection profiles, $f(x) = x^{-4.5}$ and $f(x) = x^{-3.5}$ ($\tilde{a} = 0.95$).

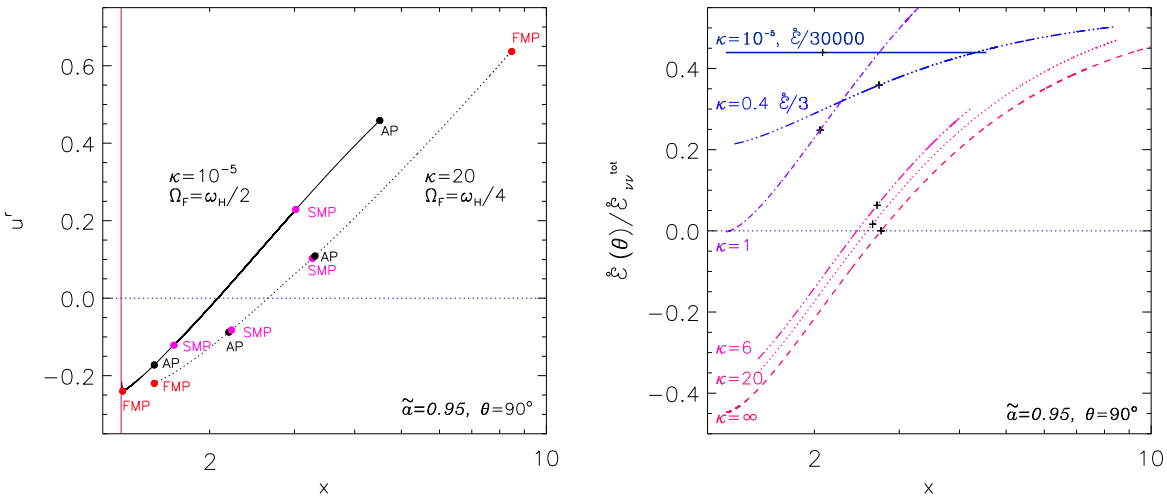

Fig. 3.— Left panel: velocity profiles of underloaded ($\kappa = 10^{-5}$) and overloaded ($\kappa = 20$) solutions, with $f(x) = x^{-4.5}$, $\tilde{a} = 0.95$, and $\theta = 90°$. The region above (below) the horizontal dotted line $u^r = 0$, corresponds to the outflow (inflow) sections. The inner and outer slow magnetosonic points (SMP), Alfvén points (AP), and fast magnetosonic points (FMP) are indicated. The vertical red line delineates the horizon. Right panel: profiles of the outflow power per solid angle for different values of the load parameter κ. The $\kappa = 10^{-5}$ and $\kappa = 0.4$ curves are rescaled for convenience. The cross symbole on each curve marks the location of the stagnation radius. In the region of the inflow where the energy flux is positive (between the point of zero flux and the stagnation point) the specific energy is negative.

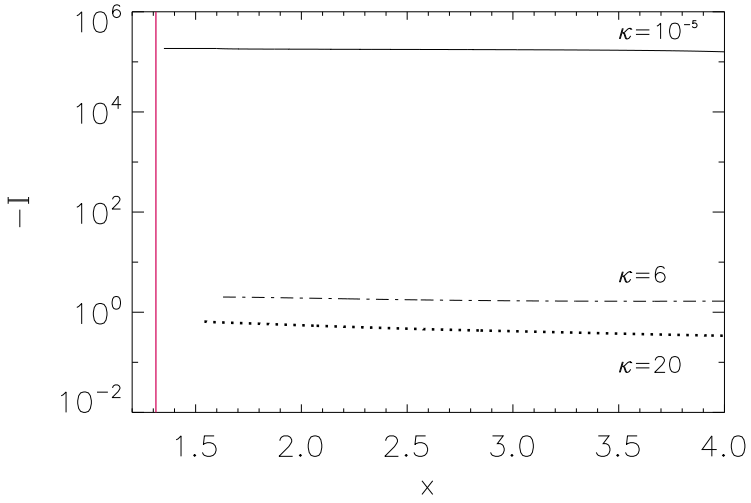

Fig. 4.— Electric current distribution, $I(x) = B_\varphi \varpi \alpha$, for equatorial flow solutions.

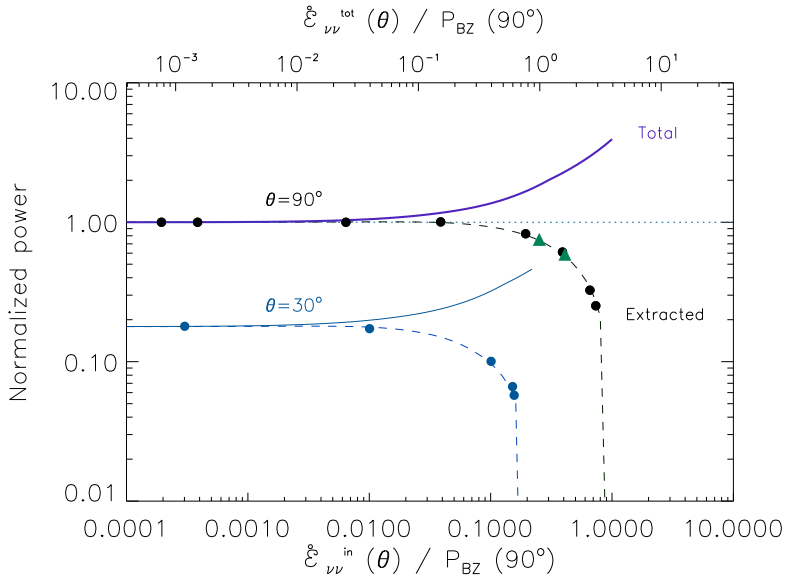

Fig. 5.— Dependence of the outflow power on the load for two different streamlines, $\theta = 90°$, and $\theta = 30°$. For reference, powers are normalized by the equatorial BZ power, $P_{BZ}(\pi/2)$, given in Equation (17). The dashed line in each case gives the normalized power per solid angle on the horizon, $\dot{\mathcal{E}}_H(\theta)/P_{BZ}(\pi/2)$, and the solid line the total power per solid angle, $\dot{\mathcal{E}}_\infty(\theta)/P_{BZ}(\pi/2)$. Specific cases are indicated by the symbols, with the circles corresponding to solutions for which $\Omega_F = \omega_H/2$, and the triangles to solutions with $\Omega_F = \omega_H/4$.

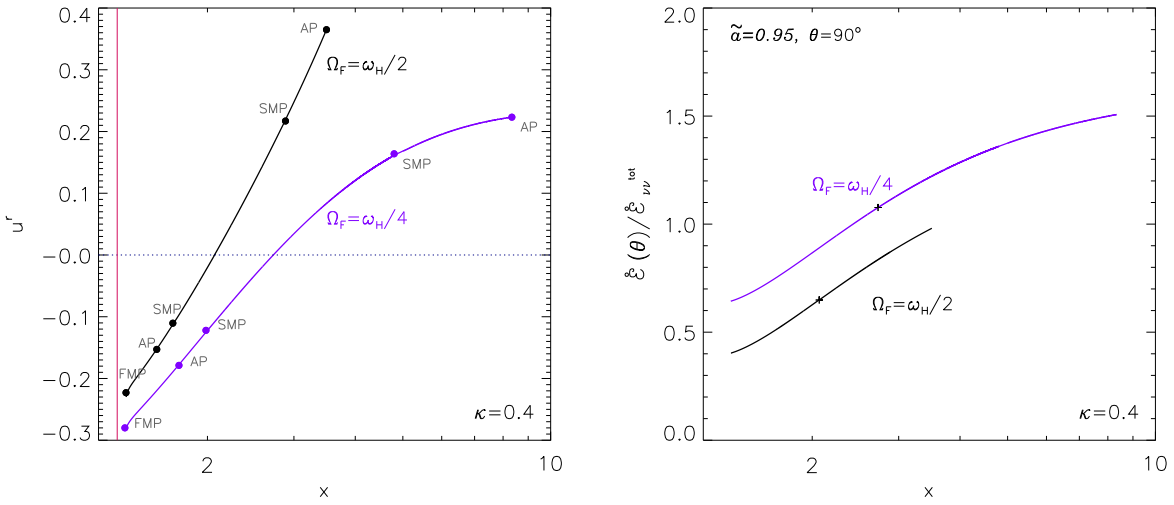

Fig. 6.— A comparison between two equatorial flow solutions with the same load parameter, $\kappa = 0.4$, and different angular velocities Ω_F, as indicated. The left panel displays the velocity profiles and the right panel the corresponding power profiles.

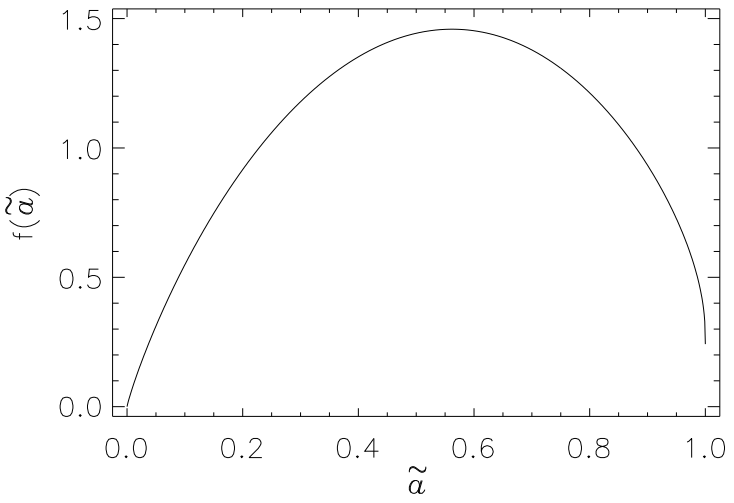

Fig. 7.— A plot of the function $f(\tilde{a})$ defined in Equation (22).

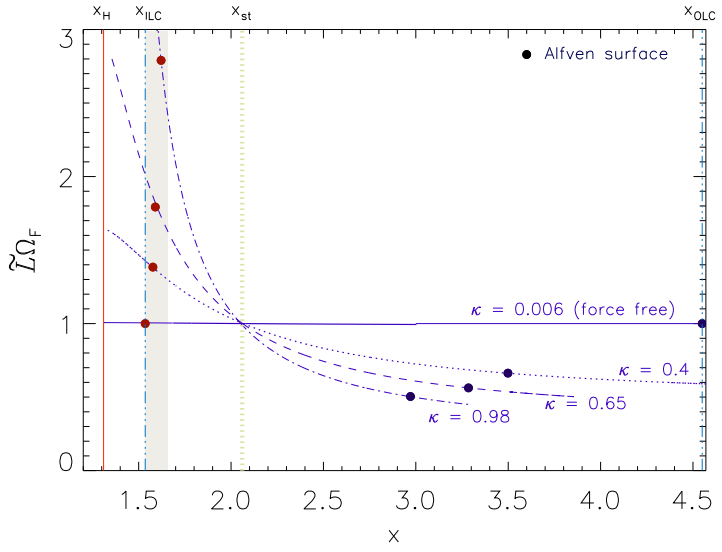

Fig. 8.— Effect of the loading efficiency on the position of the Alfvén surfaces. The profile of $\tilde{L}\Omega_F$ is shown for 4 solutions corresponding to different values of κ, and $\tilde{a} = 0.95$, $\Omega_F = \omega_H/2$. The range of Alfvén radii that allows rotational energy extraction is delineated by the shaded area. In the force-free case ($\kappa \to 0$, $\dot{\mathcal{E}}_H = P_{BZ}$) the Alfvén points coincide with the light surfaces. This result is in accord with that derived by Takahashi et al. (1990) for an adiabatic flow.